



Enhanced electron transport in rutile TiO₂ nanowires via H₂S-assisted incorporation of dissolved silicon for solar-driven water splitting

Yang Lu^{a,*}, Zi Wei^b, Nilesh P. Salke^a, Lu Yu^c, Hao Yan^a

^a Center for High Pressure Science & Technology Advanced Research, Shanghai, 201203, China

^b Department of Mechanical Engineering, University of Massachusetts Lowell, Lowell, MA, 01854, USA

^c High Magnetic Field Laboratory, Hefei Institutes of Physical Science, Chinese Academy of Sciences, Hefei, 230031, China

ARTICLE INFO

Keywords:

Titanium dioxide
Silicon doping
Charge transport
Hydrothermal reaction
Water splitting

ABSTRACT

Si-doping is an effective approach to enhance the electron transport and the photocatalytic activity of photocatalyst. In this study, for the first time the silicate glass such as fluorine-doped tin oxide (FTO) glass substrate is used as the silicon source for preparing Si-doped TiO₂ photoanodes. First, the rutile TiO₂ nanowires (NWs) were grown on FTO glass substrates by hydrothermal reaction, accompanying with the gradual dissolution of glass to generate soluble Si dopant incorporated into TiO₂ NWs. Second, the TiO₂ NWs were reduced to form the Ti³⁺ by H₂S reduction. Finally, the Si-doped TiO₂ photoanodes with higher doping density was obtained by calcination. The visible photocatalytic activity of Si-doped TiO₂ NWs photoanode towards water splitting increased about three times as compared with pure TiO₂ NWs. Reduction by H₂S resulted in the enhanced electron transport and massive increase in charge-carrier density. This work provides a novel paradigm for silicon doping in materials for accelerating their carrier transport and applications.

1. Introduction

Since the discovery of water splitting over rutile TiO₂ at half a century ago, TiO₂ semiconductors have attracted widespread interests in solar energy conversion and storage due to its unique optoelectronic properties, chemical stability, non-toxicity, and low cost [1–4]. Rutile, the thermodynamically most stable polymorph of TiO₂ commonly exhibits a prismatic or acicular shape as observed in natural minerals or artificial nanocrystals, which is favored as the fastest growth rate along [001] direction and the lowest surface energy of dominant {110} facets [5]. Besides, the electrical conductivity along [001] direction is near 10 times of that along [110] direction [6]. This anisotropy of electrical transport accompanying with preferential growth habit results in the extensive use of the one-dimensional rutile nanowires, especially the self-aligned nanowires on the substrate, in fundamental studies and real applications [5,7–15]. The photocatalytic activity of rutile photocatalyst, however, is still low. Moreover, it is widely recognized that rutile possesses a lower photoactivity than anatase partially due to its poorer electron transport, although rutile has a relatively narrower band gap of 3.0 eV to anatase (3.2 eV) [16,17].

Doping is an effective approach to alter the carrier concentration, electrical transport, surface states etc. of semiconductor photocatalysts to enhance their photocatalytic activity or photoelectrochemical (PEC)

performance [9,18–24]. In particular, doping of Si in TiO₂ lattice can improve the electron concentration, surface hydroxyl concentration, surface wettability, and in turn photoactivity [25–32]. Moreover, the electronic band structure and electron mobility of TiO₂ can also be tuned by Si-doping based on the theoretical calculation [33–35]. To date, the synthesis procedure for fabricating Si-doped TiO₂ commonly includes the material growth with the addition of silicon sources such as Si powder, SiCl₄, and ethyl silicate, which may increase the complexity and cost of synthesis [27,32,36,37]. In this work, the glass of fluorine-doped tin oxide (FTO) substrate, for the first time, is used as the silicon dopant source for preparing the Si-doped TiO₂ photoanode. We demonstrate that Si is released from the conductive glass during the hydrothermal growth of rutile nanowires and can be further incorporated into the TiO₂ lattice via H₂S treatments. The visible photoactivity of Si-doped TiO₂ nanowires photoanode increases near three times of that without H₂S treatments, which is mainly attributed to the enhanced electron transport via Si-doping. This work provides a novel approach to incorporate silicon into photocatalysts exhibiting better performance.

* Corresponding author.

E-mail addresses: yang.lu@hpstar.ac.cn, yucas@126.com (Y. Lu).

<https://doi.org/10.1016/j.apcatb.2018.12.003>

Received 20 October 2018; Received in revised form 17 November 2018; Accepted 1 December 2018

Available online 03 December 2018

0926-3373/ © 2018 Elsevier B.V. All rights reserved.

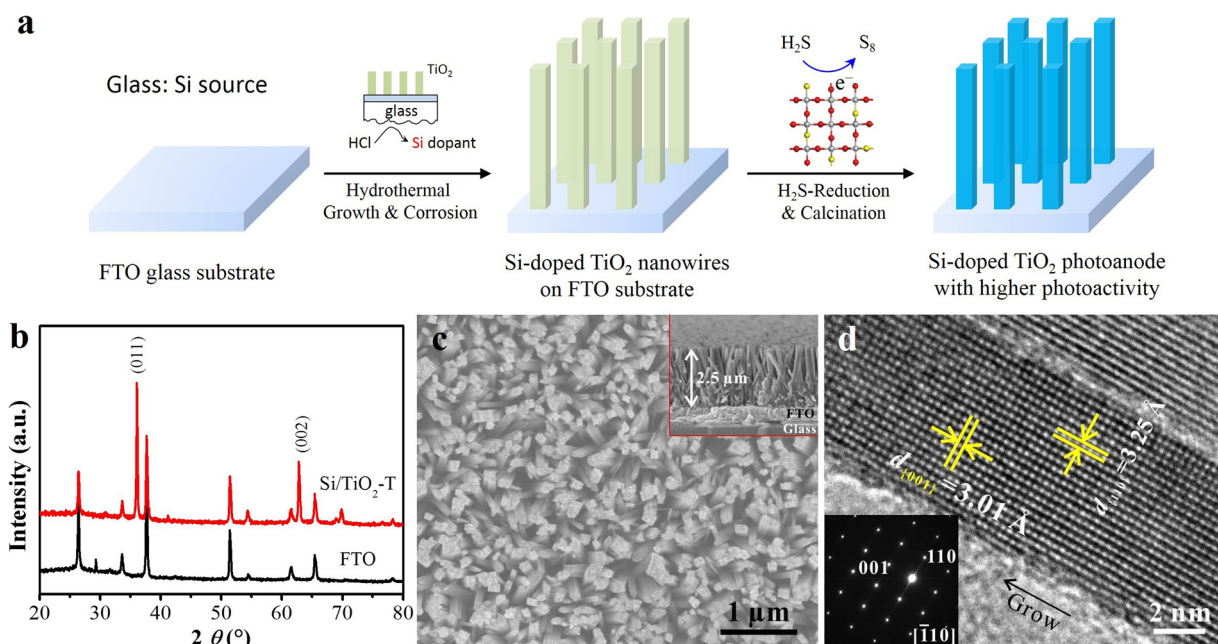


Fig. 1. (a) Scheme of doping of Si into TiO₂ NWs on FTO substrate via hydrothermal glass dissolution and H₂S treatments. (b) XRD patterns of Si-doped TiO₂ NWs photoanode (Si/TiO₂-T) and FTO substrate (FTO). (c) Representative SEM image of Si-doped TiO₂ NWs from the top view. Inset is the cross-sectional SEM image. (d) High-resolution TEM image and SAED pattern (bottom-left inset) of TiO₂ NW.

2. Experimental details

2.1. Synthesis of TiO₂ NWs on FTO substrates

The Si self-doped rutile TiO₂ nanowire array were synthesized on fluorine-doped tin oxide (FTO) glass substrates by using a hydrothermal method [13,38]. In a typical synthesis, 0.6 mL of Ti(OBu)₄ (99 wt%) was added into 50 mL of an aqueous HCl (5.0 M), under magnetic stirring in a Teflon vessel (100 mL in volume). After 5 min, four pieces of cleaned FTO substrates (7 Ω/□, 3.0 cm × 1.5 cm × 0.2 cm) were placed at an angle against the wall of the Teflon vessel with the conductive side facing down. The subsequent hydrothermal reaction was carried out at 170 °C for 6 h in an oven. After hydrothermal reaction, the autoclave was cooled naturally to room temperature. The as-synthesized electrodes were rinsed with deionized water and dried in ambient environment. The resulting sample is denoted as ‘as-synthesized TiO₂’. For comparison, the pure TiO₂ NWs was synthesized by coating the glass sides of FTO substrate with Teflon film, and other procedure and conditions are same to above.

2.2. Post-treatments of TiO₂ electrodes

The Si-doped TiO₂ photoanode with higher photoactivity was obtained by hydrothermal H₂S treatments. Briefly, 1.2 g Na₂S·9H₂O (99 wt%) and 0.6 mL acetic acid (99 wt%) were separately placed at the bottom of a Teflon vessel (100 mL in volume) by using an electrode shelf holding an as-synthesized TiO₂ electrode. Then, the Teflon vessel was quickly sealed in a stainless steel autoclave, and heated at 170 °C for 6 h. After H₂S reduction, the autoclave was cooled naturally to room temperature, and opened in fume cupboard. The electrode was taken out and washed with deionized water. Finally, the Si-doped TiO₂ electrode reduced by H₂S, denoted as Si/TiO₂-R, was calcined in muffle furnace at 500 °C for 30 min in air. The resulting sample is denoted as Si/TiO₂-T. For comparison, an as-synthesized TiO₂ electrode and the pure TiO₂ electrode were also calcined in muffle furnace at 500 °C for 30 min in air, and the resulting samples are denoted as Si/TiO₂ and Pure-TiO₂, respectively.

2.3. Characterization

The structure and morphologies of samples were investigated with TEM (JEM-2010), XRD (X’Pert Pro MPD), and FESEM (Hitachi SU8020). The elemental composition was measured by XPS (Thermo ESCALAB 250) with Al K_α X-ray as the excitation source and all the XPS spectra were calibrated by the C 1s signal to the binding energy of 284.6 eV. The dissolved Si content in hydrothermal solution was quantified by inductively couple plasma (ICP) after filtration. UV–vis absorption spectra were carried out on a UV–vis spectrophotometer (Shimadzu, UV-2700). The electron paramagnetic resonance (EPR) measurements were carried out using a Bruker EMX plus 10/12 CW spectrometer at 9.407705 GHz, equipped with a continuous He gas-flow cryostat to control the temperature at 80 K.

2.4. Photoelectrochemical measurements

Photoelectrochemical measurements were conducted in a three-electrode configuration, where Pt mesh and Ag/AgCl (saturated KCl) were used as counter and reference electrode, respectively. Electrolyte was 0.10 M NaNO₃ aqueous solution (pH = 7.0). A 350 W Xe arc lamp was employed as a visible light source with a 400 nm cut-off filter (CHF-XM-350 W, Beijing Trusttech Co. Ltd., China). The IPCE spectra were measured with wavelength range from 300 to 500 nm. The Mott-Schottky (MS) experiments were performed in the dark. The intensity modulated photovoltage/photocurrent spectroscopy (IMVS/IMPS) were measured by using an electrochemical workstation (Zennium, Zahner) under a modulated light emitting diodes (λ = 395 nm) driven by a source supply (Zahner, Germany).

3. Results and discussion

3.1. Preparation and characterization of Si-doped TiO₂ nanowires photoanode

Fig. 1a schematically illustrates the incorporation of Si into TiO₂ nanowires grown on FTO substrate via hydrothermal glass dissolution and H₂S treatments (including Reduction and Calcination). In details,

the self-aligned rutile TiO_2 nanowires (NWs) were grown on FTO glass substrates by the hydrothermal method as used elsewhere [14,15,39]. During the hydrothermal procedure, however, the glass of the FTO substrate could be corroded, accompanying with soluble silicic species releasing. Meanwhile, the silicic species, such as orthosilicic acid, could be embedded into TiO_2 voids or marginally doped into lattice. Finally, the treatments of the TiO_2 nanowires by H_2S reduction followed with calcination could lead to dramatic incorporation of Si into the rutile lattice, which is based on the existing oxygen vacancies or Ti^{3+} promote the ion bonding to crystal lattice [40,41]. Fig. 1b shows the X-ray diffraction (XRD) patterns of Si-doped TiO_2 NWs after H_2S -treatments (denoted by $\text{Si/TiO}_2\text{-T}$) photoanode and FTO glass substrate. The diffraction peaks of (011) and (002) are corresponding to the rutile TiO_2 crystal structure (JCPDS no. 96-900-4142), consisting with the XRD pattern of rutile TiO_2 nanowires photoanode reported previously [13,42]. Fig. 1c shows the representative scanning electron microscopy (SEM) images of $\text{Si/TiO}_2\text{-T}$ photoanode from the top view and cross-sectional view (inset), respectively. SEM images confirm the nearly uniform growth of NWs. The mean length and diameter of these Si-doped TiO_2 NWs were approximately 2.5 μm and 200 nm. Fig. 1d shows the typical high-resolution transmission electron microscopy (TEM) image and selected area electron diffraction (SAED) of $\text{Si/TiO}_2\text{-T}$ NW. The SAED pattern as well as (110) interplanar distance of 3.25 Å and (001) interplane distance of 3.01 Å indicate the Si-doped TiO_2 NWs are of rutile phase exposed with predominant {110} facets and grown preferentially along [001] growth direction.

The surface composition and chemical states of $\text{Si/TiO}_2\text{-T}$ and the calcined counterpart without H_2S -reduction (denoted by Si/TiO_2) were characterized by X-ray photoelectron spectroscopy (XPS) as shown in Fig. 2. The Si 2p spectra of samples (Fig. 2a) reveals that the binding energy of Si 2p for $\text{Si/TiO}_2\text{-T}$ NWs is 102.0 eV, which is slightly smaller than that of Si/TiO_2 NWs (102.2 eV) and SiO_2 (103.4 eV) [30,36]. As Ti has a larger affinity for oxygen than Si, the formation of the Si-O-Ti band in $\text{Si/TiO}_2\text{-T}$ sample results in the shift of binding energy to a lower value [30]. Fig. 2b and c shows the Ti 2p and O 1s spectra of Si/

TiO_2 and $\text{Si/TiO}_2\text{-T}$. The binding energies of Ti 2p_{3/2} peak and O 1s peak for $\text{Si/TiO}_2\text{-T}$ are 458.8 eV and 529.9 eV, respectively, ~0.2 eV higher than Si/TiO_2 . The shifts of 0.2–0.4 eV in both Ti peaks and O peaks to the higher binding energy from Si/TiO_2 to $\text{Si/TiO}_2\text{-T}$ are due to the greater electronegativity of Si via O acting on Ti. For pure TiO_2 , the binding energy of Ti 2p_{3/2} peak is around 458.2 eV and lower than that of Si/TiO_2 (458.6 eV) [43]. Besides, Fig. 2d indicates the valence band of $\text{Si/TiO}_2\text{-T}$ slightly shifts to the negative potential with 0.2 eV as compared with Si/TiO_2 , implying the improved oxidation capability after H_2S -reduction. These results suggested the formation of Si-O-Ti bond in TiO_2 samples and the Si-doping amount of $\text{Si/TiO}_2\text{-T}$ was ca. 1.0 atomic% (Fig. S1 and S2).

To insight into the doping mechanism, the hydrothermal erosion of glass and the formation of Si-doped TiO_2 NWs were systematically studied. Fig. 3a and b show the SEM images of the back side of the as-synthesized photoanode glass substrate and a pristine FTO glass substrate, respectively. There are lots of traces in the back side of the photoanode glass, suggesting the FTO glass in the solution was etched during the hydrothermal synthesis of TiO_2 nanowires. Then, the Si complex would dissolve into the hydrothermal solution. The concentration of Si in the solution after reaction for preparing four photoanodes is approximately 19.11 ppm, which was determined by inductively coupled plasma (ICP) (See Supporting Information Table S1). In addition, the concentration of dissolved Si in solution could be easily increased by immersing more FTO conductive glass slices or other silicate glass slices into the reacting solution (Table S1), in other words, the dissolved Si was generally undetectable in previous report using less FTO substrates (usually one slice) based on the same synthesis procedures due to its lower concentration, or it may be ignored. Consequently, the effect of FTO glass etching could not be neglected when a large scale production of TiO_2 NWs photoanodes was achieved using the hydrothermal method.

To the best of our knowledge, there was no report about the rutile TiO_2 nanowires or nanorods photoanode doped with Si elements from the FTO glass substrate synthesized by hydrothermal reaction. While

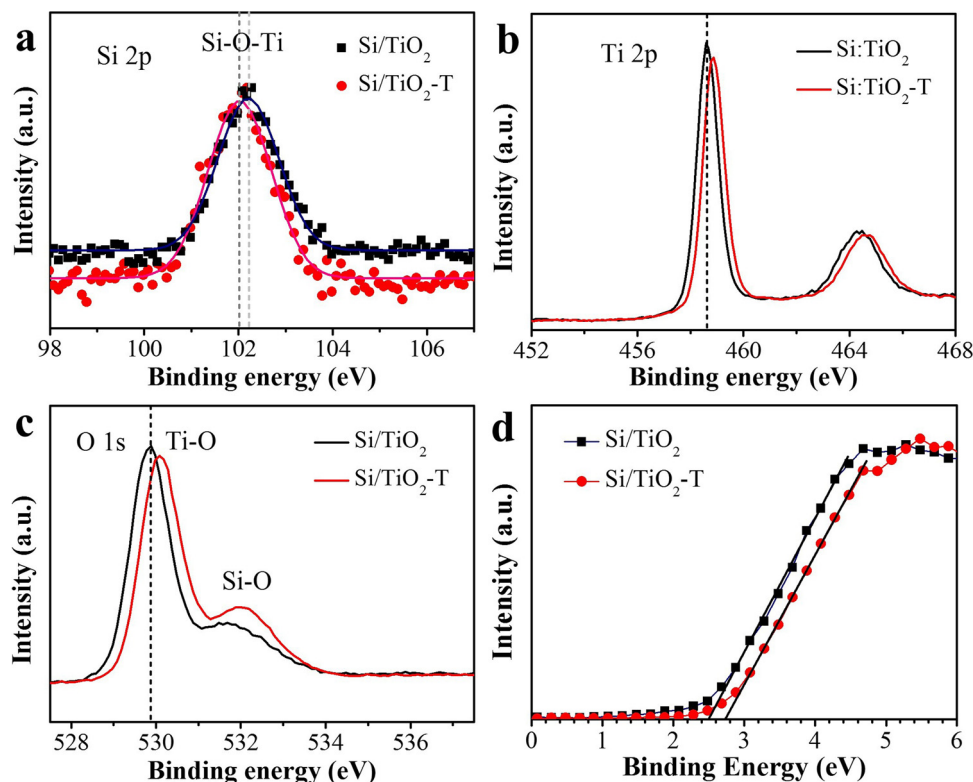


Fig. 2. (a–d) XPS spectra of Si 2p, Ti 2p, O 1s, and the valence band of Si/TiO_2 sample and $\text{Si/TiO}_2\text{-T}$ sample.

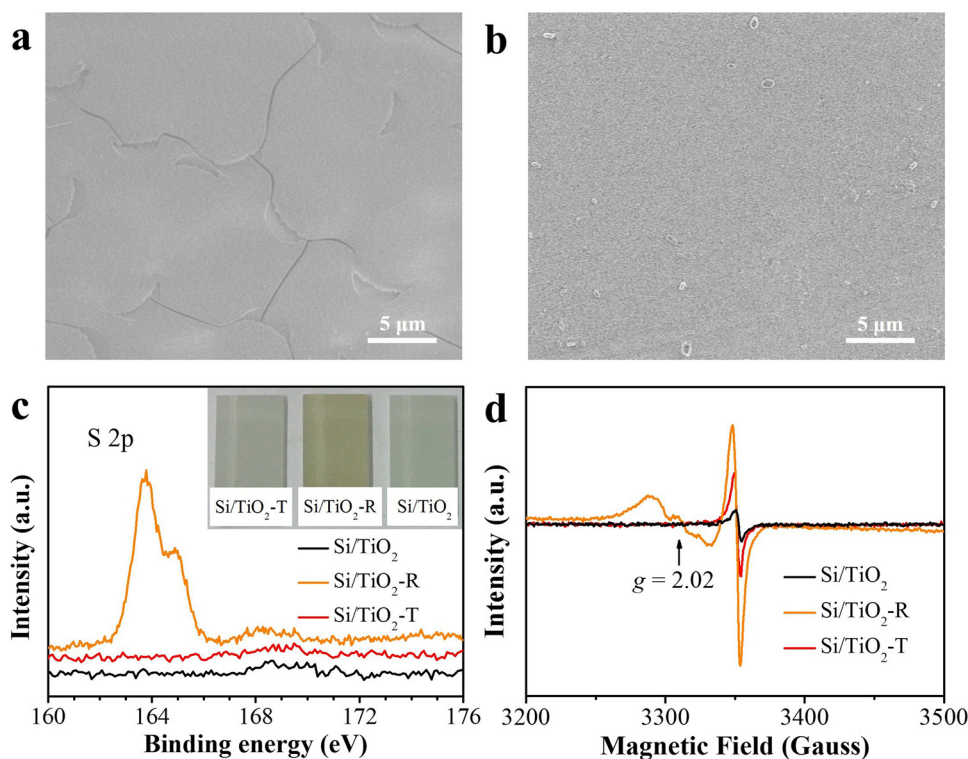
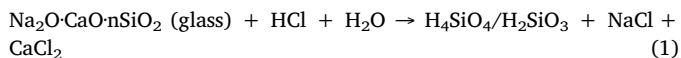


Fig. 3. (a) and (b) SEM images of the back sides of the FTO glass substrate underwent hydrothermal reaction and the pristine FTO glass substrate, respectively. (c) S 2p XPS spectra and photograph (inset) of samples under different treatment conditions. (d) EPR spectra recorded at 80 K under a dark condition for samples with different treatments.

glass is generally corrosion-resistant to chemical attack, yet glass does undergo chemical changes, depending on conditions of exposure [44]. In our case, the immersed glass substrates could be dramatically corroded by the highly acidic solution under high temperature and pressure. The chemical formation of silicic species in the solution is believed to be orthosilicic acid (H_4SiO_4) or metasilicic acid (H_2SiO_3) based on following corrosion reaction:



The silicon source could be partially doped into TiO₂ lattice or transformed into SiO₂ by calcination in air of as-synthesized TiO₂ NWs, and the Si-doping density could be further increased by H₂S reduction followed by calcination. As shown in Fig. 3c, the surface of TiO₂ photoanode after H₂S-reduction without calcination (denoted by Si/TiO₂-R) is yellow. The S 2p spectrum of samples revealed the yellow species is elemental sulfur (S⁰), which can be fully removed by calcination treatment. The emerging of S⁰ implied the TiO₂ NWs were reduced to form Ti³⁺, which were investigated by low-temperature electron paramagnetic resonance (EPR). Fig. 3d shows the strong EPR signals at g = 2.003 for Si/TiO₂, Si/TiO₂-T, and Si/TiO₂-R samples were observed, which were assigned to the electrons trapped on oxygen vacancies [40,45]. The presence of the signal at g = 2.02 for the Si/TiO₂-R sample reduced by H₂S was corresponding to O₂⁻ produced from the reduction of adsorbed O₂ from the air by surface Ti³⁺, confirming the presence of surface Ti³⁺ after H₂S reduction treatment [46,47]. The existing Ti³⁺ or oxygen vacancies will promote the Si bonding to the TiO₂ NWs [40,41].

3.2. Visible PEC water oxidation performance

The photoelectrochemical water oxidation performances of the Si/TiO₂-T photoanode were evaluated in 0.10 M NaNO₃ aqueous solution under visible light. Fig. 4a shows the voltammograms of Si/TiO₂-T photoanode under different visible light intensities. It can be seen that the photocurrent (I_{ph}) for Si/TiO₂-T photoanode under the dark condition is negligible. With the increased light intensity, the photocurrent

increased accordingly. The transient photocurrent response curves for Si/TiO₂-T photoanode are shown in Fig. 4b, which suggest the chemical and structural stability of Si/TiO₂-T photoanode for PEC water oxidation is excellent. To estimate the effect of H₂S treatments on the photocatalytic activity of TiO₂ NWs, the voltammograms of Si/TiO₂ photoanode under various visible light intensities were performed and shown in Fig. 4c. Comparatively, the minimum applied potential to reach plateau photocurrent decreased by ~0.24 eV when the TiO₂ photoanode underwent H₂S treatments. Fig. 4d shows the plateau photocurrent over light intensity ($I_{\text{ph}}-\varphi$) linear relationships derived from Fig. 4(a) and (c) at +0.80 V a slope of 8.24×10^{-4} A/W for Si/TiO₂-T is 2.81 times of Si/TiO₂ (2.93×10^{-4} A/W), which exhibits the superior photocatalytic activity of Si-doped photoanode treated by H₂S. In addition, the photocurrent of Si/TiO₂-T photoanode, exhibiting the long-term stability, is ca. 3.2 times of Pure-TiO₂ photoanode at +0.80 V (Fig. S3a and c).

3.3. Mechanism of performance enhancement

To determine the photoactivity as a function of wavelength, the incident photon-to-current conversion efficiencies (IPCE) were collected at 0 V vs Ag/AgCl. IPCE can be described using the equation [48]

$$\text{IPCE}(\lambda) = \eta_{\text{charge}}(\lambda) \times \eta_{\text{transport}}(\lambda) \times \eta_{\text{transfer}}(\lambda) \quad (2)$$

where $\eta_{\text{charge}}(\lambda)$, $\eta_{\text{transport}}(\lambda)$, $\eta_{\text{transfer}}(\lambda)$ represent the efficiencies of charge (e^- and h^+) generation, charge transport inside the material, and charge transfer at the photoanode/electrolyte interface. IPCE spectra (Fig. 5a) shows that the Si/TiO₂-T photoanode exhibited higher IPCE values than that of Si/TiO₂ photoanode at the wavelength range of 325–420 nm, which agrees that the Si-doping, especially for higher doping density, increases the quantum efficiency of TiO₂ [27]. Similar results were discovered in TiO₂ NWs after doping with H, N, Sn, and oxygen vacancies [12,49–51]. The UV–vis absorption spectra (Fig. 5b) shows the blue shift of adsorption edge for TiO₂ sample after H₂S treatments, i.e., the optical bandgap of Si/TiO₂-T was broadened as compared with Si/TiO₂ sample, which is consistent with previous reports [26,31,36,37]. Therefore, the superior performance of Si/TiO₂-T

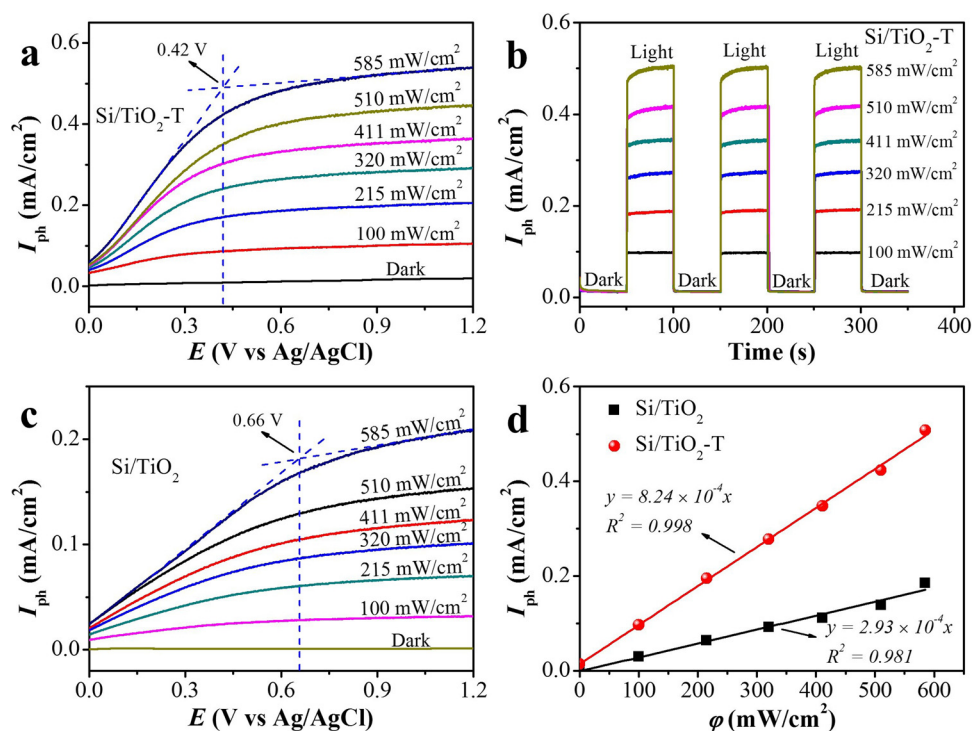


Fig. 4. (a) and (c) Voltammograms obtained from Si/TiO₂ and Si/TiO₂-T photoanodes in 0.10 M NaNO₃ aqueous solution under different visible light intensities, respectively. (b) Transient photocurrent responses recorded from Si/TiO₂-T photoanode applied +0.80 V potential bias under different visible light intensities. (d) I_{ph} - ϕ relationships derived from Fig. 4(a) and (c) at +0.80 V.

photoanode is ascribed to the enhanced electron transport.

As mentioned above, Si-doping in the TiO₂ lattice can improve the electron concentration and mobility. Therefore, Mott-Schottky plots of samples were measured in the dark. As shown in Fig. 5c, the positive slopes in the plots demonstrate the Si/TiO₂ and Si/TiO₂-T NWs are all n-type semiconductor. The donor densities of samples can be calculated from Fig. 5c using Mott-Schottky relation

$$N_d = \left(\frac{2}{e_0 \epsilon \epsilon_0} \right) / \left[\frac{d(1/C^2)}{dV} \right] \quad (3)$$

Where N_d is the donor density, e_0 is the electron charge, ϵ_0 is the permittivity of vacuum, ϵ is the dielectric constant ($\epsilon = 170$ for rutile TiO₂). [52] As marked in Fig. 5c, the donor density (N_d) of $4.49 \times 10^{18} \text{ cm}^{-3}$ for the Si/TiO₂-T NWs is 15.1 times that of Si/TiO₂ NWs ($2.98 \times 10^{17} \text{ cm}^{-3}$). The donor density of the pure rutile TiO₂ NWs (Pure-TiO₂) is of $2.47 \times 10^{17} \text{ cm}^{-3}$, which is smaller than the Si/TiO₂-T and Si/TiO₂ NWs (Fig. S3b). Hence, the Mott-Schottky studies

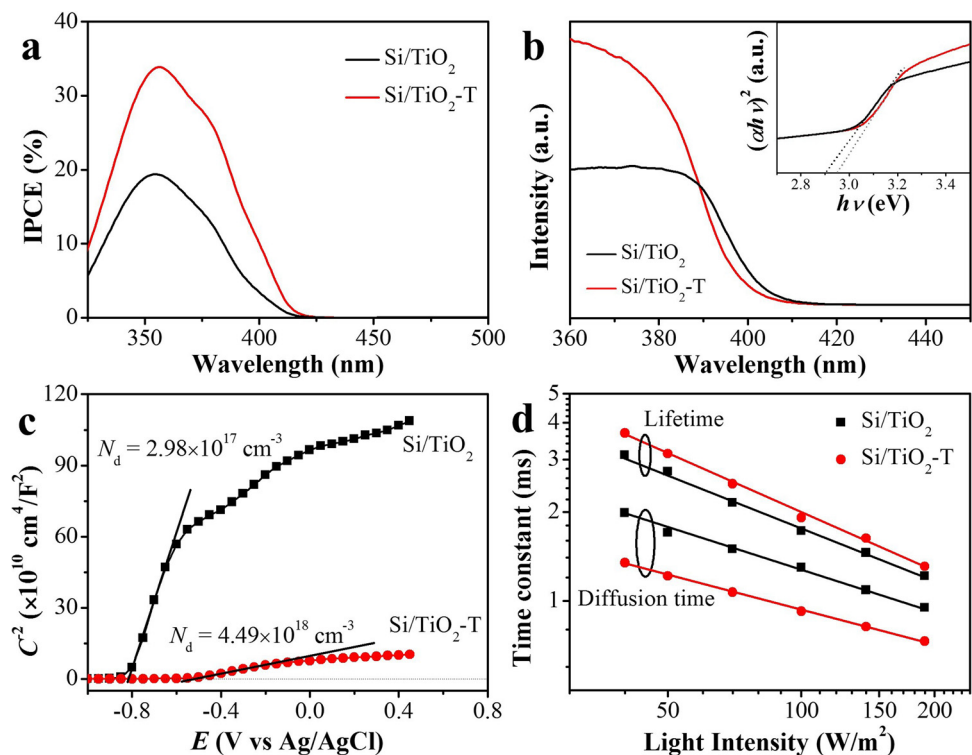


Fig. 5. (a) IPCE spectra for Si/TiO₂ and Si/TiO₂-T photoanodes collected at 0 V vs Ag/AgCl. (b) UV-vis absorption spectra of samples. The inset is the corresponding transformed Kubelka-Munk function $(\alpha h\nu)^2$ vs $h\nu$ for Si/TiO₂ and Si/TiO₂-T samples. (c) Mott-Schottky plots of Si/TiO₂ and Si/TiO₂-T photoanodes. (d) Incident light intensity dependent electron diffusion time and lifetime constant in Si/TiO₂ and Si/TiO₂-T photoanodes.

imply that Si-doping in TiO₂ NWs via H₂S-treatments leads to 18.2 times increase in the charge-carrier density, which is better than N and Ti(III) doping [27,28,52–55]. Furthermore, the intensity modulated photocurrent/photovoltage spectroscopy (IMPS/IMVS) were used to determine the electron lifetime and diffusion time of Si/TiO₂ and Si/TiO₂-T photoanodes. Fig. 5d compares the time constants of light intensity dependent electron diffusion (IMPS) and charge recombination (IMVS) in Si/TiO₂ and Si/TiO₂-T photoanodes. For both photoanodes, the time constant shows a power-law dependence on the light intensity. The diffusion times of Si/TiO₂-T photoanode are shorter than that of Si/TiO₂ photoanode, which imply the larger electron diffusion coefficients of Si/TiO₂-T [56]. In addition, the lifetimes of Si/TiO₂-T photoanode are slightly longer than that of Si/TiO₂ photoanode. These results suggest that the enhanced electron transport in Si-doped TiO₂ via H₂S treatments is responsible for the superior performance for visible PEC water oxidation.

4. Conclusions

The Si self-doped rutile TiO₂ nanowires array were directly synthesized on FTO glass substrates by hydrothermal method. The glass substrates were used as the source of oxoanion groups such as SiO₃²⁻ due to its partial corrosion in the hydrothermal reaction solution. According to the formation of Ti³⁺ in H₂S-reduced TiO₂, the Si-doped TiO₂ photoanodes with higher donor density were prepared via H₂S reduction and calcination. The visible light photocatalytic activity of Si-doped TiO₂ photoanode towards photoelectrochemical water oxidation is about three times of pure TiO₂ photoanode and Si-doped TiO₂ photoanode without H₂S reduction, which was ascribed to the enhanced electron transport, i.e., higher charge-carrier density, longer electron lifetime, and larger diffusion coefficient in Si-doped TiO₂ NWs. This work not only provides a facile strategy to prepare Si-doped materials using the silicate glass as a doping source but also offers clues for the improving of photocatalysis activity.

Acknowledgments

This work is financially supported by the National Nature Science Foundation of China (NSFC) (Grant No. U1530402). A portion of this work was performed on the Steady High Magnetic Field Facilities, High Magnetic Field Laboratory, CAS. We acknowledge Dr. W. Tong at CHMFL for the EPR measurements and data analysis. Y.L. would like to thank the Hefei Institutes of Physical Science (ISSP), where the preliminary experimental work was carried out. We are grateful to Freyja O'Toole of HPSTAR for editing this manuscript.

Appendix A. Supplementary data

Supplementary material related to this article can be found, in the online version, at doi:<https://doi.org/10.1016/j.apcatb.2018.12.003>.

ICP measurement of reaction solution with dissolved Si, XPS and EDX analysis of samples, the I-V and Mott-Schottky plot of pure rutile TiO₂ NWs, and the long-term stability of photoelectrode are supplied as Supporting Information.

References

- [1] Y. Wang, H. Suzuki, J. Xie, O. Tomita, D.J. Martin, M. Higashi, D. Kong, R. Abe, J. Tang, *Chem. Rev.* 118 (2018) 5201–5241.
- [2] X. Zhang, Y. Wang, B. Liu, Y. Sang, H. Liu, *Appl. Catal. B: Environ.* 202 (2017) 620–641.
- [3] A.L. Linsebigler, G.Q. Lu, J.T. Yates, *Chem. Rev.* 95 (1995) 735–758.
- [4] M. Pelaez, N.T. Nolan, S.C. Pillai, M.K. Seery, P. Falaras, A.G. Kontos, P.S.M. Dunlop, J.W.J. Hamilton, J.A. Byrne, K. O'Shea, M.H. Entezari, D.D. Dionysiou, *Appl. Catal. B: Environ.* 125 (2012) 331–349.
- [5] X.D. Wang, Z.D. Li, J. Shi, Y.H. Yu, *Chem. Rev.* 114 (2014) 9346–9384.
- [6] O. Byl, J.T. Yates, *J. Phys. Chem. B* 110 (2006) 22966–22967.
- [7] V. Jordan, V.D.B.C. Dasireddy, B. Likozar, A. Podgornik, A. Rečnik, *Cryst. Growth Des.* 18 (2018) 4484–4494.
- [8] L.K. Dhandole, M.A. Mahadik, S.G. Kim, H.S. Chung, Y.S. Seo, M. Cho, J.H. Ryu, J.S. Jang, *ACS Appl. Mater. Interfaces* 9 (2017) 23602–23613.
- [9] G. Sahasrabudhe, J. Krizan, S.L. Bergman, R.J. Cava, J. Schwartz, *Chem. Mater.* 28 (2016) 3630–3633.
- [10] B.A. Aragaw, C.-J. Pan, W.-N. Su, H.-M. Chen, J. Rick, B.-J. Hwang, *Appl. Catal. B: Environ.* 163 (2015) 478–486.
- [11] B. Liu, H.M. Chen, C. Liu, S.C. Andrews, C. Hahn, P. Yang, *J. Am. Chem. Soc.* 135 (2013) 9995–9998.
- [12] M. Xu, P. Da, H. Wu, D. Zhao, G. Zheng, *Nano Lett.* 12 (2012) 1503–1508.
- [13] B. Liu, E.S. Aydil, *J. Am. Chem. Soc.* 131 (2009) 3985–3990.
- [14] X.J. Feng, K. Shankar, O.K. Varghese, M. Paulose, T.J. Latempa, C.A. Grimes, *Nano Lett.* 8 (2008) 3781–3786.
- [15] Y. Liu, Y. Li, F. Peng, Y. Lin, S. Yang, S. Zhang, H. Wang, Y. Cao, H. Yu, *Appl. Catal. B: Environ.* 241 (2019) 236–245.
- [16] T. Luttrell, S. Halpegamage, J. Tao, A. Kramer, E. Sutter, M. Batzill, *Sci. Rep.* 4 (2014).
- [17] N.G. Park, J. van de Lagemaat, A.J. Frank, *J. Phys. Chem. B* 104 (2000) 8989–8994.
- [18] J.J.M. Vequizo, H. Matsunaga, T. Ishiku, S. Kamimura, T. Ohno, A. Yamakata, *ACS Catal.* 7 (2017) 2644–2651.
- [19] Z. Wang, B. Wen, Q. Hao, L.M. Liu, C. Zhou, X. Mao, X. Lang, W.J. Yin, D. Dai, A. Selloni, X. Yang, *J. Am. Chem. Soc.* 137 (2015) 9146–9152.
- [20] M.A. Lukowski, J. Song, *J. Phys. Chem. C* 115 (2011) 12388–12395.
- [21] X. Zhang, X. Quan, S. Chen, Y. Zhang, *J. Hazard. Mater.* 177 (2010) 914–917.
- [22] I. Cesar, A. Kay, J.A.G. Martinez, M. Gratzel, *J. Am. Chem. Soc.* 128 (2006) 4582–4583.
- [23] I.H. Lee, J.J. Lee, P. Kung, F.J. Sanchez, M. Razeghi, *Appl. Phys. Lett.* 74 (1999) 102–104.
- [24] P. Guan, H. Bai, C. Li, Y. Ge, D. Xu, B. Chen, T. Xia, W. Fan, W. Shi, *Adv. Mater. Interfaces* 5 (2018) 1701574.
- [25] E.M. Golden, N.C. Giles, S. Yang, L.E. Halliburton, *Phys. Rev. B* 91 (2015) 134110.
- [26] M.N. Asiah, M.H. Mamat, Z. Khushaimi, S. Abdullah, M. Rusop, A. Qurashi, *Microelectron. Eng.* 136 (2015) 31–35.
- [27] H.S. Kim, D.T. Nguyen, E.-C. Shin, J.-S. Lee, S.K. Lee, K.-S. Ahn, S.H. Kang, *Electrochim. Acta* 114 (2013) 159–164.
- [28] M. Sun, X. Zhang, J. Li, X. Cui, D. Sun, Y. Lin, *Electrochem. commun.* 16 (2012) 26–29.
- [29] D.N. Bui, S.Z. Kang, X. Li, J. Mu, *Catal. Commun.* 13 (2011) 14–17.
- [30] R. Jin, Z. Wu, Y. Liu, B. Jiang, H. Wang, *J. Hazard. Mater.* 161 (2009) 42–48.
- [31] Y. Su, S. Chen, X. Quan, H. Zhao, Y. Zhang, *Appl. Surf. Sci.* 255 (2008) 2167–2172.
- [32] X. Yan, J. He, D.G. Evans, X. Duan, Y. Zhu, *Appl. Catal. B: Environ.* 55 (2005) 243–252.
- [33] Y. Lin, Z. Jiang, C. Zhu, X. Hu, X. Zhang, H. Zhu, J. Fan, H.L. Sheng, *Appl. Catal. B: Environ.* 142–143 (2013) 38–44.
- [34] W. Shi, Q. Chen, Y. Xu, D. Wu, C.-f. Huo, *J. Solid State Chem.* 184 (2011) 1983–1988.
- [35] K. Yang, Y. Dai, B. Huang, *Chem. Phys. Lett.* 456 (2008) 71–75.
- [36] Z. Lu, X. Jiang, B. Zhou, X. Wu, L. Lu, *Appl. Surf. Sci.* 257 (2011) 10715–10720.
- [37] N. Bao, Z. Wei, Z. Ma, F. Liu, G. Yin, *J. Hazard. Mater.* 174 (2010) 129–136.
- [38] I.S. Cho, Z. Chen, A.J. Forman, D.R. Kim, P.M. Rao, T.F. Jaramillo, X. Zheng, *Nano Lett.* 11 (2011) 4978–4984.
- [39] Q. Zeng, J. Bai, J. Li, L. Li, L. Xia, B. Zhou, Y. Sun, *Appl. Energy* 220 (2018) 127–137.
- [40] T.Q. Lin, C.Y. Yang, Z. Wang, H. Yin, X.J. Lu, F.Q. Huang, J.H. Lin, X.M. Xie, M.H. Jiang, *Energy Environ. Sci.* 7 (2014) 967–972.
- [41] A. Folger, P. Ebbinghaus, A. Erbe, C. Scheu, *ACS Appl. Mater. Interfaces* 9 (2017) 13471–13479.
- [42] C. Huang, J. Bian, R.-Q. Zhang, *J. Phys. Chem. C* 121 (2017) 18892–18899.
- [43] Y.L. Lin, T.J. Wang, J. Yong, *Powder Technol.* 123 (2002) 194–198.
- [44] C.H. Hahner, I.C. Gardner, U.S. Government Printing Office (1949).
- [45] I. Nakamura, N. Negishi, S. Kutsuna, T. Ihara, S. Sugihara, E. Takeuchi, *J. Mol. Catal. A Chem.* 161 (2000) 205–212.
- [46] S.M. Prokes, J.L. Gole, X.B. Chen, C. Burda, W.E. Carlos, *Adv. Funct. Mater.* 15 (2005) 161–167.
- [47] M. Anpo, M. Che, B. Fubini, E. Garrone, E. Giamello, M.C. Paganini, *Top. Catal.* 8 (1999) 189–198.
- [48] Z.B. Chen, T.F. Jaramillo, T.G. Deutsch, A. Kleiman-Shwarsstein, A.J. Forman, N. Gaillard, R. Garland, K. Takanabe, C. Heske, M. Sunkara, E.W. McFarland, K. Domen, E.L. Miller, J.A. Turner, H.N. Dinh, *J. Mater. Res.* 25 (2010) 3–16.
- [49] I.S. Cho, M. Logar, C.H. Lee, L. Cai, F.B. Prinz, X. Zheng, *Nano Lett.* 14 (2014) 24–31.
- [50] G. Wang, H. Wang, Y. Ling, Y. Tang, X. Yang, R.C. Fitzmorris, C. Wang, J.Z. Zhang, Y. Li, *Nano Lett.* 11 (2011) 3026–3033.
- [51] S. Hoang, S. Guo, N.T. Hahn, A.J. Bard, C.B. Mullins, *Nano Lett.* 12 (2012) 26–32.
- [52] C. Mao, F. Zuo, Y. Hou, X. Bu, P. Peng, *Angew. Chem. Int. Ed.* 53 (2014) 10485–10489.
- [53] G. Wang, X. Xiao, W. Li, Z. Lin, Z. Zhao, C. Chen, C. Wang, Y. Li, X. Huang, L. Miao, C. Jiang, Y. Huang, X. Duan, *Nano Lett.* 15 (2015) 4692–4698.
- [54] P. Guan, H. Bai, F. Wang, H. Yu, D. Xu, B. Chen, T. Xia, W. Fan, W. Shi, *ChemCatChem* 10 (2018) 4927–4933.
- [55] P. Guan, H. Bai, F. Wang, H. Yu, D. Xu, W. Fan, W. Shi, *Chem. Eng. J.* 358 (2019) 658–665.
- [56] J. van de Lagemaat, A.J. Frank, *J. Phys. Chem. B* 105 (2001) 11194–11205.